



massachusetts institute of technology — computer science and artificial intelligence laboratory

---

# An Expectation Maximization Approach for Integrated Registration, Segmentation, and Intensity Correction

Kilian M. Pohl, John Fisher,  
W. Eric L. Grimson & William M. Wells

AI Memo 2005-010

April 2005

**Abstract.** This paper presents a statistical framework which combines the registration of an atlas with the segmentation of MR images. We use an Expectation Maximization-based algorithm to find a solution within the model, which simultaneously estimates image inhomogeneities, anatomical labelmap, and a mapping from the atlas to the image space. An example of the approach is given for a brain structure-dependent affine mapping approach. The algorithm produces high quality segmentations for brain tissues as well as their substructures. We demonstrate the approach on a set of 30 brain MR images. In addition, we show that the approach performs better than similar methods which separate the registration from the segmentation problem.

## 1 Introduction

With notable exceptions, segmentation and registration have been recognized as two separate problems in medical imaging research. However, these techniques complement each other. For example, segmentation simplifies the registration of anatomical structures with ambiguous intensity patterns [1]. On the other hand, aligning an atlas to these anatomical structures aids the detection of indistinct boundaries and therefore simplifies the segmentation problem [2]. In this paper, we describe a simultaneous solution to both problems by combining them in a unified Bayesian framework.

The idea of the unified Bayesian framework was motivated by boundary localization techniques, such as [3, 4], which align an atlas to the subject and simultaneously estimate the shape of a structure. These methods relate both problems to each other by extending the definition of the shape to include its pose. This paper suggests an integrated segmentation and registration approach for voxel-based classification methods. In contrast to boundary localization approaches, voxel-based classification methods consider the anatomical structure associated with each voxel within a Bayesian framework.

Voxel-based classification methods have coupled registration and segmentation of misaligned spectral images [5, 6]. However, we wish to align an atlas to MR images and separate the images into anatomical structures. Previous voxel-based classification methods perform this task sequentially [7–10, 2]. The separation of these two issues increases the risk of systematic biases [11, 12, 1]. In contrast, our new approach is based on the principle of least commitment so that an initial imperfect estimation converges to a good approximation for each problem.

This paper is based on an instance of the Expectation Maximization Algorithm (EM) by Wells [13]. Unlike boundary localization techniques, this method explicitly models the image inhomogeneities of MR images. Therefore, the approach can segment large data sets without manual intervention. However, the approach of Wells [13] cannot differentiate structures with similar intensity patterns as it uses stationary characteristics of anatomical structure. To overcome this drawback, Section 2 proposes a Bayesian framework which describes the relationship between atlas registration, intensity correction, and image segmentation. This formulation is based on a maximum a posteriori estimation formulation whose solution gives an approximation to these three interrelated problems.

Section 3 applies the concept to a hierarchical registration framework modelling global- and structure-dependent deformations. The limits and benefits of the implementation are illustrated in Section 4 by applying it to synthetic images. We then present a study comparing the robustness of our algorithm with respect to other EM implementations which outline a set of 30 MR images into the major brain tissue classes as well as the thalamus, a structure with indistinct boundaries.

## 2 Deriving an EM Framework for Simultaneous Inhomogeneity Correction, Registration, and Segmentation

The accuracy of outlining structures with indistinct boundaries on MR images with tissue classification methods significantly depends on properly modeling the image inhomogeneities as well as correctly registering the atlas to the subject. In this section, we develop a unified framework which performs segmentation, registration and inhomogeneity correction simultaneously.

### 2.1 A Maximum a Posteriori Estimation Problem for the Three Instances

As mentioned above, correctly modeling the image inhomogeneities and accurately mapping the atlas to the image space greatly influences the robustness of atlas based segmenters. Due to their complex dependencies, it is very difficult to extract the inhomogeneities  $\mathcal{B}$  and the registration parameters  $\mathcal{R}$  from the MR images  $I$  without additional assumptions.

However, this problem is greatly simplified when formulated as an incomplete data problem within an EM framework. To determine  $\mathcal{B}$  and  $\mathcal{R}$  within this framework, we define the following MAP estimation problem over the incomplete data model:

$$(\hat{\mathcal{B}}, \hat{\mathcal{R}}) = \arg \max_{\mathcal{B}, \mathcal{R}} \log P(\mathcal{B}, \mathcal{R} | I). \quad (1)$$

In general, this results in a system of equations for which there is no analytical solution.

To simplify the problem, we combine the observed image intensities  $I$  with the unknown true segmentation  $\mathcal{T}$ . If  $\mathcal{T}$  is known,  $\mathcal{B}$  and  $\mathcal{R}$  can more easily be estimated from  $I$ . We now restate Equation (1) by marginalizing over the missing data  $\mathcal{T}$

$$(\hat{\mathcal{B}}, \hat{\mathcal{R}}) = \arg \max_{\mathcal{B}, \mathcal{R}} \log \left( \sum_{\mathcal{T}} P(\mathcal{B}, \mathcal{R}, \mathcal{T} | I) \right) \quad (2)$$

Next, we incorporate  $P(\mathcal{T} | I, \mathcal{B}', \mathcal{R}')$ , where  $(\mathcal{B}', \mathcal{R}')$  are estimates of  $(\hat{\mathcal{B}}, \hat{\mathcal{R}})$ , into Equation (2) and define  $E_{A|B}(f(C)) \triangleq \sum_A P(A|B)f(C)$  to get the following relationship

$$(\hat{\mathcal{B}}, \hat{\mathcal{R}}) = \arg \max_{\mathcal{B}, \mathcal{R}} \log \left( \sum_{\mathcal{T}} \frac{P(\mathcal{B}, \mathcal{R}, \mathcal{T} | I) P(\mathcal{T} | I, \mathcal{B}', \mathcal{R}')}{P(\mathcal{T} | I, \mathcal{B}', \mathcal{R}')} \right) = \arg \max_{\mathcal{B}, \mathcal{R}} \log E_{\mathcal{T} | I, \mathcal{B}', \mathcal{R}'} \left( \frac{P(\mathcal{B}, \mathcal{R}, \mathcal{T} | I)}{P(\mathcal{T} | I, \mathcal{B}', \mathcal{R}')} \right)$$

The purpose of these operations is to put Equation (2) into a form such that we can exploit the following bound derived via Jensen's Inequality as in [14]

$$\log E_{\mathcal{T} | I, \mathcal{B}', \mathcal{R}'} \left( \frac{P(\mathcal{B}, \mathcal{R}, \mathcal{T} | I)}{P(\mathcal{T} | I, \mathcal{B}', \mathcal{R}')} \right) \geq E_{\mathcal{T} | I, \mathcal{B}', \mathcal{R}'} \left( \log \frac{P(\mathcal{B}, \mathcal{R}, \mathcal{T} | I)}{P(\mathcal{T} | I, \mathcal{B}', \mathcal{R}')} \right) \quad (3)$$

The right side of Equation (3), which defines a lower bound on the objective function  $\log E_{\mathcal{T}|I, \mathcal{B}', \mathcal{R}'} \left( \frac{P(\mathcal{B}, \mathcal{R}, \mathcal{T}|I)}{P(\mathcal{T}|I, \mathcal{B}', \mathcal{R}')} \right)$ , is more easily maximized using an EM implementation. When properly defined, the EM framework [14] gives two important guarantees. First, each iteration yields an improved estimate of  $(\mathcal{B}, \mathcal{R})$  as measured by Equation (1). Second, the algorithm converges to a local maxima of the objective function. In our case, the Maximization Step (M-Step) is defined by the update rule:

$$\begin{aligned}
(\mathcal{B}', \mathcal{R}') &\leftarrow \arg \max_{\mathcal{B}, \mathcal{R}} E_{\mathcal{T}|I, \mathcal{B}', \mathcal{R}'} (\log P(\mathcal{B}, \mathcal{R}, \mathcal{T}|I) - \log P(\mathcal{T}|I, \mathcal{B}', \mathcal{R}')) \\
&= \arg \max_{\mathcal{B}, \mathcal{R}} E_{\mathcal{T}|I, \mathcal{B}', \mathcal{R}'} (\log P(\mathcal{B}, \mathcal{R}|\mathcal{T}, I) + \log P(\mathcal{T}|I)) \\
&= \arg \max_{\mathcal{B}, \mathcal{R}} E_{\mathcal{T}|I, \mathcal{B}', \mathcal{R}'} (\log P(I|\mathcal{T}, \mathcal{B}, \mathcal{R}) + \log P(\mathcal{B}, \mathcal{R}|\mathcal{T}) - \log P(I|\mathcal{T})) \\
&= \arg \max_{\mathcal{B}, \mathcal{R}} E_{\mathcal{T}|I, \mathcal{B}', \mathcal{R}'} (\log P(I|\mathcal{T}, \mathcal{B}, \mathcal{R}) + \log P(\mathcal{R}|\mathcal{T}, \mathcal{B}) + \log P(\mathcal{B}|\mathcal{T}))
\end{aligned} \tag{4}$$

The optimization procedure decomposes nicely as consequences of the following independence assumptions: First, we assume independence of  $I$  with respect to  $\mathcal{R}$  conditioned on  $\mathcal{T}$  and  $\mathcal{B}$  following Wells [13]. We therefore characterize each anatomical structure with a stationary intensity distribution which is not influenced by the mapping between atlas and image space. Based on the same argument, we also assume independence of  $\mathcal{R}$  with respect to  $\mathcal{B}$  conditioned  $\mathcal{T}$ . Finally, we assume independence of  $\mathcal{B}$  with respect to  $\mathcal{T}$  as the image inhomogeneities are caused by the radio frequency coil of the scanner [8]. Thus, Equation (4) simplifies to

$$(\mathcal{B}', \mathcal{R}') \leftarrow \arg \max_{\mathcal{B}, \mathcal{R}} E_{\mathcal{T}|I, \mathcal{B}', \mathcal{R}'} (\log P(I|\mathcal{T}, \mathcal{B}) + \log P(\mathcal{R}|\mathcal{T}) + \log P(\mathcal{B})) \tag{5}$$

The unknown true segmentation  $\mathcal{T} = (\mathcal{T}_1, \dots, \mathcal{T}_n)$  is composed of the indicator random variables  $\mathcal{T}_x \in \{e_1, \dots, e_N\}$ , where  $x$  represents a voxel on the image grid. The vector  $e_a$  is zero at every position but  $a$ , where its value is one. For example, if  $\mathcal{T}_x = e_a$  then voxel  $x$  is assigned to the anatomical structure  $a$ . If we now define

$$\mathcal{W}_x(a) \triangleq E_{\mathcal{T}_x|I_x, \mathcal{B}'_x, \mathcal{R}'_x} (\mathcal{T}_x(a)) = 1 \cdot P(\mathcal{T}_x = e_a|I_x, \mathcal{B}'_x, \mathcal{R}'_x) + 0 \cdot P(\mathcal{T}_x(a) \neq e_a|I_x, \mathcal{B}'_x, \mathcal{R}'_x)$$

In order to further reduce the computational complexity of the model we make two additional independence assumptions. Based on the previous discussion, we assume that  $\mathcal{R}$  is independent of  $\mathcal{B}$  and we assume spatial independence of the unknown ground-truth  $\mathcal{T}$ . A simple application of Bayes' rule yields:

$$\mathcal{W}_x(a) = \frac{P(I_x|\mathcal{T}_x(a)=e_a, \mathcal{B}'_x, \mathcal{R}'_x) \cdot P(\mathcal{T}_x(a)=e_a|\mathcal{B}'_x, \mathcal{R}'_x)}{P(I_x|\mathcal{B}'_x, \mathcal{R}'_x)} = \frac{P(I_x|\mathcal{T}_x(a)=1, \mathcal{B}'_x) \cdot P(\mathcal{T}_x(a)=1|\mathcal{R}'_x)}{P(I_x|\mathcal{B}'_x, \mathcal{R}'_x)} \tag{6}$$

Equation (5) simplifies to

$$(\mathcal{B}', \mathcal{R}') \leftarrow \arg \max_{\mathcal{B}, \mathcal{R}} \sum_x \sum_{\alpha} \mathcal{W}_x(a) (\log P(I|\mathcal{T}_x = e_a, \mathcal{B}) + \log P(\mathcal{R}|\mathcal{T}_x = e_a)) + \log P(\mathcal{B})$$

and M-Step solves the following two separate MAP problems

$$\mathcal{R}' \leftarrow \arg \max_{\mathcal{R}} \sum_x \sum_{\alpha} \mathcal{W}_x(a) \cdot \log P(\mathcal{T}_x = e_a|\mathcal{R}) + \log P(\mathcal{R}) \tag{7}$$

$$\mathcal{B}' \leftarrow \arg \max_{\mathcal{B}} \sum_x \sum_{\alpha} \mathcal{W}_x(a) \cdot \log P(I|\mathcal{T}_x = e_a, \mathcal{B}) + \log P(\mathcal{B}) \tag{8}$$

We must point out that a minor drawback of this formulation is its sensitivity towards uncommon characteristics favored by the atlas. The aligned atlas is represented in Equation (7) and Equation (6) by the conditional probability  $P(\mathcal{T}_x = e_a | \mathcal{R})$ . To match the atlas with the segmentation problem, the algorithm compensates for any biases through intensity correction and atlas realignment. For example, if the atlas does not properly capture the intensity distribution defined through the image acquisition protocol, the algorithm might not be able to distinguish the intensity pattern of the neck with those inside the brain. The image inhomogeneity correction will try to correct for any image artifacts inside the neck area to increase the similarity between neck and brain. In addition, the registration approach might scale the atlas of brain tissue to cover both brain and neck. Thus, the algorithm converges to a suboptimal solution but recalibration of the atlas intensity distributions can overcome this problem.

In summary, we find a local maxima to the difficult MAP problem of Equation (1) by solving the simpler Equation (4), which is embedded in an EM framework. Based on independence assumptions, the E-Step determines  $\mathcal{W}$  of Equation (6) and the M-Step solves for the MAP estimates of Equation (7) and Equation (8).

## 2.2 Defining a Hierarchical Registration Approach

To solve the MAP estimation problem of Equation (7), we first define the registration parameters  $\mathcal{R}$  and the conditional log likelihood  $\log P(\mathcal{T} | \mathcal{R})$ . The parameters  $\mathcal{R}$  model a hierarchical registration framework, which distinguishes between global- and structure-dependent deformations. We then apply the registration framework to the MAP estimation problem and find a solution with another optimization algorithm.

The hierarchical registration parameters  $\mathcal{R}$  capture the correspondence between atlas, brain, and structures within the brain. The mapping of the atlas to the image space is performed by an interpolation function  $r(\mathcal{R}, x)$ , which maps voxel  $x$  into the coordinate system defined by  $\mathcal{R}$ .  $r(\mathcal{R}, \cdot)$  can be rigid, affine or non-rigid. As a rigid registration can be interpreted as special case of an affine transformation, we now focus our discussion on affine and non-rigid registration methods.

The parameters  $\mathcal{R}$  can be structure-dependent or -independent. Structure-independent parameters capture the correspondence between atlas and image space. Restrained by an affine interpolation, the degrees of freedom of  $\mathcal{R}$  are too low to capture the characteristics of individual brain structures ([11, 12]). The alternative is a non-rigid framework which often has problems aligning structures with indistinct boundaries [1].

Structure-dependent registration parameters treat the relationship between the atlas and image space for each structure independently. Since most of the misalignment is structure-independent, e.g the head of the patient is not aligned with the atlas space, we expect small differences between structure-dependent parameters of different structures. However, forcing the parameters to be similar across structures is difficult to express in Equation (7).

We model dependency across structures with a hierarchical registration framework  $\mathcal{R} = (\mathcal{R}_G, \mathcal{R}_S)$ .  $\mathcal{R}_G$  are the global registration parameters, which describe the non-structure dependent deformations between atlas and image. The structure dependent parameters  $\mathcal{R}_S \triangleq (\mathcal{R}_1, \dots, \mathcal{R}_N)$  are the residual structure-specific deformations that are not adequately explained by  $\mathcal{R}_G$ . The similarity between different structure specific

parameters is encoded in Equation (7) through the prior probability  $P(\mathcal{R})$ . In Section 3 we define  $\mathcal{R}$  explicitly and then model  $P(\mathcal{R})$  with a simple Gaussian distribution. The distributions enforce tight bounds on  $\mathcal{R}_S$  and weak constraints on  $\mathcal{R}_G$ .

Let  $\mathcal{R}_a$  of  $\mathcal{R}_S$  be the parameters specific to structure  $a$  with  $a \in \{1, \dots, N\}$ . If we now define  $f_a$  as the spatial distribution of structure  $a$  in the atlas space, then  $f_a(r(\mathcal{R}_G, \mathcal{R}_a, \cdot))$  defines the spatial distribution in the structure specific coordinate system of the patient. Thus, we can model the conditional structure probability:

$$P(\mathcal{T}_x = e_a | \mathcal{R}) \triangleq \frac{f_a(r(\mathcal{R}_G, \mathcal{R}_a, x))}{\sum_{a'} f_{a'}(r(\mathcal{R}_G, \mathcal{R}_{a'}, x))} \quad (9)$$

Substituting Equation (9) into Equation (7) changes the MAP problem to

$$\begin{aligned} \mathcal{R} &\leftarrow \arg \max_{\mathcal{R}} \sum_x \sum_a [\mathcal{W}_x(a) \cdot (\log f_a[r(\mathcal{R}_G, \mathcal{R}_a, x)] - \log \sum_{a'} f_{a'}[r(\mathcal{R}_G, \mathcal{R}_{a'}, x)])] \\ &\quad + \log P(\mathcal{R}) \\ &= \arg \max_{\mathcal{R}} \sum_x [\sum_a (\mathcal{W}_x(a) \cdot \log f_a[r(\mathcal{R}_G, \mathcal{R}_a, x)] - \log (\sum_{a'} f_{a'}[r(\mathcal{R}_G, \mathcal{R}_{a'}, x)]))] \\ &\quad + \log P(\mathcal{R}) \end{aligned} \quad (10)$$

Finding a closed form solution to Equation (10) is generally difficult. Instead, we express Equation (10) through a objective function  $Q(\cdot)$  for which the maximum is found in Section 3. We also replace  $\log f_a(r(\mathcal{R}_G, \mathcal{R}_a, x))$  by  $\log(f_a(r(\mathcal{R}_G, \mathcal{R}_a, x)) + \epsilon)$  with  $\epsilon > 0$ , so that the MAP problem is defined for  $f_a(r(\mathcal{R}_G, \mathcal{R}_a, x)) = 0$ . If we define

$$Q(\mathcal{R}) \triangleq \sum_x \sum_a [\mathcal{W}_x(a) \cdot \log(f_a[r(\mathcal{R}_G, \mathcal{R}_a, x)] + \epsilon)] - \log (\sum_{a'} f_{a'}[r(\mathcal{R}_G, \mathcal{R}_{a'}, x)] + \epsilon) + \log P(\mathcal{R})$$

then Equation (10) becomes

$$\mathcal{R}' \leftarrow \arg \max_{\mathcal{R}} Q(\mathcal{R}) \quad (11)$$

To get a better understanding of the objective function  $Q(\cdot)$ , let  $y_a \triangleq r(\mathcal{R}_G, \mathcal{R}_a, x)$  be the coordinate of voxel  $x$  in the atlas space of structure  $a$ . If now voxel  $x$  is clearly assigned to structure  $a'$  then  $\mathcal{W}_x(a') = 1$ ,  $f_{a'}(y_{a'}) = \sum_a f_a(y_a)$  so that

$$\sum_a [\mathcal{W}_x(a) \log(f_a(y_a) + \epsilon)] - \log(f_{a'}(y_{a'}) + \epsilon) = \log(f_{a'}(y_{a'}) + \epsilon) - \log(f_{a'}(y_{a'}) + \epsilon) = 0.$$

Thus, the value of  $Q(\cdot)$  is not influenced by  $x$  as the sum over all structures at this voxel is zero. In other words,  $Q(\cdot)$  is determined by all voxels that are not clearly assigned to one structure.

### 2.3 Estimating the Intensity Inhomogeneities

The calculations of the inhomogeneities  $\mathcal{B}$  closely follow [13]. In Equation (8), the conditional intensity distribution of structure  $a$  for  $n$  input channels is now defined as

$$P(I_x | \mathcal{T}_x = e_a, \mathcal{B}_x) \triangleq \frac{1}{\sqrt{(2 \cdot \pi)^n |\Upsilon_a|}} e^{-\frac{1}{2} (I_x - \mathcal{B}_x - \mu_a)^T \cdot \Upsilon_a^{-1} \cdot (I_x - \mathcal{B}_x - \mu_a)}$$

We define  $A_x(a) \triangleq \frac{\partial}{\partial \mathcal{B}_x} P(I_x | \mathcal{T}_x = e_a, \mathcal{B}_x) = \Upsilon_a^{-1} \cdot (I_x - \mathcal{B}_x - \mu_a)$  to turn Equation (8) into a closed form solution for  $\mathcal{B}'$  yielding

$$0 = \sum_x \mathcal{W}_x \cdot \frac{\partial}{\partial \mathcal{B}_x} \log P(I_x | \mathcal{T}_x, \mathcal{B}_x) + \frac{\frac{\partial}{\partial \mathcal{B}_x} P(\mathcal{B})}{P(\mathcal{B})} = \mathcal{W}_x^T \cdot A_x + \frac{\frac{\partial}{\partial \mathcal{B}_x} P(\mathcal{B})}{P(\mathcal{B})}$$

for which a solution can be approximated. In practice, we achieve very good results by defining the approximation according to [13] which estimates  $\mathcal{B}$  via a low pass filter applied to a weighted residual that depends on  $\mathcal{W}$ ,  $(\mu_a, \Upsilon_a)$ , and  $I$  [11, 15].

## 2.4 EM Applied to the Registration and Segmentation Problem

Section 2 developed an EM implementation. The E-Step calculates  $\mathcal{W}$  of Equation (6) based on the aligned spatial priors  $f_a(r(\mathcal{R}'_G, \mathcal{R}'_a, \cdot))$ , intensity  $I$ , image inhomogeneities  $\mathcal{B}'$ , and voxel  $x$

$$\begin{aligned} \mathcal{W}_x(a) &= \frac{P(I_x | \mathcal{T}_x(a)=1, \mathcal{B}'_x) P(\mathcal{T}_x(a)=1 | \mathcal{R}')}{P(I_x | \mathcal{B}'_x, \mathcal{R}')} = \frac{P(I_x | \mathcal{T}_x(a)=1, \mathcal{B}'_x) \cdot P(\mathcal{T}_x(a)=1 | \mathcal{R}')}{\sum_{a'} P(I_x | \mathcal{T}_x(a)=1, \mathcal{B}'_x) \cdot P(\mathcal{T}_x(a)=1 | \mathcal{R}')} \\ &= \frac{|\Upsilon_a|^{-0.5} \cdot e^{-\frac{1}{2}(I_x - \mathcal{B}'_x - \mu_a)^T \cdot \Upsilon_a^{-1} \cdot (I_x - \mathcal{B}'_x - \mu_a)} \cdot f_a(r(\mathcal{R}'_G, \mathcal{R}'_a, x))}{\sum_{a'} |\Upsilon_{a'}|^{-0.5} \cdot e^{-\frac{1}{2}(I_x - \mathcal{B}'_x - \mu_{a'})^T \cdot \Upsilon_{a'}^{-1} \cdot (I_x - \mathcal{B}'_x - \mu_{a'})} \cdot f_{a'}(r(\mathcal{R}'_G, \mathcal{R}'_{a'}, x))} \end{aligned}$$

The M-Step updates the approximation of the inhomogeneities  $\mathcal{B}'$  and registration parameters  $\mathcal{R}'$  based on the current weights  $\mathcal{W}$ . The inhomogeneity  $\mathcal{B}$  is approximated by the product between the simple low pass filter  $H$ , now represented by a large matrix, and a weighted residuum (see [13]):

$$\mathcal{B}' \leftarrow H \cdot \sum_a \mathcal{W}_x(a) \Upsilon_a^{-1} (I_x - \mu_a)$$

$\mathcal{R}'$  is updated by the maximum of objective functions  $Q(\cdot)$  as defined in Equation (11)

$$\mathcal{R}' \leftarrow \arg \max_{\mathcal{R}} Q(\mathcal{R})$$

To find the maximum we use a maximization algorithm as discussed in the next section.

## 3 Affine Registration Implementation

This section describes an implementation of the approach presented in Section 2.4. We will give an example of an interpolation function  $r(\cdot, \cdot, \cdot)$ , the corresponding registration parameters  $\mathcal{R}$ , a Probability Density Function (PDF)  $p(\mathcal{R})$ , and a maximization algorithm to solve the MAP estimation problem defined in Equation (11).

The interpolation function  $r(\cdot, \cdot, \cdot)$  of Equation (11) can model various mapping approaches. For simplicity, we choose an affine interpolation function so that the parameters for  $\mathcal{R}_z = (\vec{t}_z^t, \vec{r}_z^t, \vec{s}_z^t)^t$  with  $z \in \{G, 1, \dots, N\}$  define translation  $\vec{t}_z$ , rotation  $\vec{r}_z$ , and scaling  $\vec{s}_z$ . The mapping is defined as  $r(\cdot, \cdot, \cdot) : R^{12 \times 12 \times 3} \rightarrow R^3, (\mathcal{R}_g, \mathcal{R}_a, x) \rightarrow$

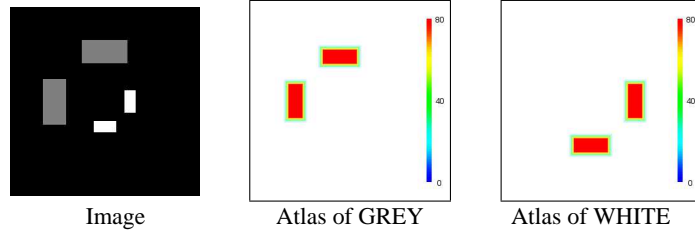


**Fig. 1.** The structures of the foreground - GREY and WHITE - are of different scale in the image but not in the atlas space. To secure statistical consistency within our affine warping framework the atlas of the background, which is black in the image, is implicitly defined by the foreground.

$A_{\mathcal{R}_G} \cdot A_{\mathcal{R}_a} \cdot (x^t, 1)^t$  where  $A_{\mathcal{R}_z}$  is an affine transformation matrix based on the parameter setting  $\mathcal{R}_z$ .

This framework makes no assumptions about the correspondence between the atlas and the image space by uniformly distributing the global registration parameter  $\mathcal{R}_g$ . As opposed to  $\mathcal{R}_g$ , the structure specific parameters  $\mathcal{R}_S \triangleq (\mathcal{R}_1, \dots, \mathcal{R}_N)$  describe the residual of structure specific deformations that are not well explained by  $\mathcal{R}_G$ . In general, our model should penalize large deviations of  $\mathcal{R}_S$  from the expected mean, which is approximated by the average structure-specific registration parameters of the training data. We enforce this penalty by modeling the PDF of  $\mathcal{R}_S$  as a Gaussian distribution  $N(\mu_{\mathcal{R}_S}, \Upsilon_{\mathcal{R}_S})$  with structure independent mean  $\mu_{\mathcal{R}_S}$  and variance  $\Upsilon_{\mathcal{R}_S}$  based on the mapping parameters of the training data. We choose a Gaussian distribution as small variance  $\Upsilon_{\mathcal{R}_S}$  discourages large deformations from the mean  $\mu_{\mathcal{R}_S}$ . In addition, Gaussian distributions simplify the calculations in the M-Step [16].

Based on the previous modeling assumptions the cost function is defined as

$$Q(\mathcal{R}) \triangleq \sum_x \left( \sum_a (\mathcal{W}_x(a) \cdot \log [f_a(A_{\mathcal{R}_G} \cdot A_{\mathcal{R}_a} \cdot (x^t, 1)^t) + \epsilon]) \right. \\ \left. - \log \left[ \sum_a f_a(A_{\mathcal{R}_G} \cdot A_{\mathcal{R}_a} \cdot (x^t, 1)^t) + \epsilon \right] \right) - \frac{1}{2} (\mathcal{R}_S - \mu_{\mathcal{R}_S})^t \Upsilon_{\mathcal{R}_S}^{-1} (\mathcal{R}_S - \mu_{\mathcal{R}_S})$$

A problem illustrating this approach is shown in Figure 1. WHITE and GREY are defined by spatial distributions of equivalent size but their scale in image space differs. The black structure, the background (BG), is the opposite of the foreground composed by WHITE and GREY. The affine registration parameters of BG are too constrained to cope with the enlarged WHITE and shrunken GREY object. To solve this problem and therefore increase the statistical consistency of the model, the spatial distribution of BG is determined implicitly. If we define the structure-specific coordinates in the atlas space as  $y_a \triangleq A_{\mathcal{R}_G} \cdot A_{\mathcal{R}_a} \cdot (x^t, 1)^t$  then the spatial distribution of BG is

$$f_{BG}(x) \triangleq \begin{cases} 1 - \sum_{a \neq BG} f_a(y_a) & , \text{if } \sum_{a \neq BG} f_a(y_a) < 1 \\ 0 & , \text{otherwise} \end{cases}$$

so that the cost function changes to



$$Q(\mathcal{R}) \triangleq \sum_x \left( \sum_{a \neq BG} \mathcal{W}_x(a) \cdot \log [f_a(y_a) + \varepsilon] + \mathcal{W}_x(BG) \cdot \log \left[ \sum_{a \neq BG} f_a(y_a) + \varepsilon \right] \right. \\ \left. - \log \left[ \sum_{a \neq BG} f_a(y_a) + f_{BG}(x) + \varepsilon \right] \right) - \frac{1}{2} (\mathcal{R}_S - \mu_{\mathcal{R}_S})' \Upsilon_{\mathcal{R}_S}^{-1} (\mathcal{R}_S - \mu_{\mathcal{R}_S}) \quad (12)$$

In order to find a solution to the MAP problem defined by  $Q(\cdot)$ , we first decouple the search for  $\mathcal{R}_G$  and  $\mathcal{R}_S$  as dependencies between these two parameter settings can cause instability. We then estimate the solution to these problems with the help of a maximization algorithms that find the optimal solution without the derivative of  $Q(\cdot)$ . Such methods include the Downhill Simplex algorithm and the Powell’s method [17]. We complete this section with the pseudo code below which describes the integration of the Powell’s method into our implementation.

---

**Algorithm 1:** SEGMENTATION AND REGISTRATION()

---

**repeat**

**E-Step:** Update soft assignment of anatomical structures

$$\mathcal{W}_x(a) \leftarrow \frac{1}{2} P(I_x | \mathcal{T}_x(a) = 1, \mathcal{B}'_x) \cdot f_a(r(\mathcal{R}'_G, \mathcal{R}'_a, x))$$

**M-Step:** Update parameter space

$$\mathcal{B}' \leftarrow H \cdot \sum_a \mathcal{W}_x(a) \Upsilon_a^{-1} (I_x - \mu_a)$$

$$\mathcal{R}'_G \leftarrow \text{Result of Powell's method with } Q((\cdot, \mathcal{R}'_S))$$

$$\mathcal{R}'_S \leftarrow \text{Result of Powell's method with } Q((\mathcal{R}'_G, \cdot))$$

**until**  $\mathcal{B}'$  and  $\mathcal{R}'$  converge

**define** labelmap:  $\mathcal{T}_x \leftarrow \arg \max_a \mathcal{W}_x(a)$

---

## 4 Validation

This section evaluates our method in two steps. The first experiment applies variations of the implementation discussed in Section 3 to synthetic images. The second study uses a 30 Brain MR image set to evaluate different mapping strategies of the atlas to the image space within an EM segmentation framework.

### 4.1 Experiment on Synthetic Images

To illustrate the reliability of our approach, we apply different variations of the implementation discussed in Section 3 to synthetic images similar as in Figure 1. The images are composed of three structures WHITE, GREY, and BLACK. Unlike in Figure 1 WHITE and GREY have the same intensity pattern (see Figure 2). All structure specific parameters stay fixed with the exception of WHITE in the image space.

The robustness of the variations of our implementation is tested with respect to the scaling of structure WHITE in the synthetic image. The structure is scaled within a

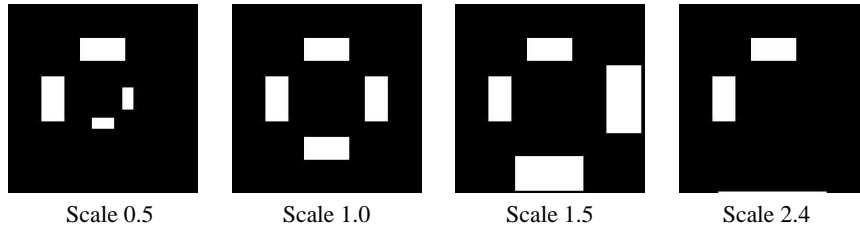


**Fig. 2.** The test images are examples of our experiment, which tests the robustness of various implementations from Section 3. In this experiment, only the scale of object WHITE changes. The atlas space of Figure 1 remains constant and corresponds to the image with scale 1.0.

range of 0.1 to 2.4 of its original size for which the atlas space in Figure 1 was constructed. For each test image, the automatically generated segmentations are compared to the ground truth by using the volume overlap measure of Dice [18].

The first experiment shown in Figure 3 (a) compares the reliability of our approach using Powell’s to one using the Downhill Simplex method. Powell’s method outperforms Downhill Simplex method, when comparing their robustness with respect to the scaling of structure WHITE. The Downhill Simplex method fails on images where WHITE and the non-aligned atlas (Figure 1) do not overlap. Powell’s method is unreliable for scaling parameters greater than 2.4 for whom WHITE almost disappears from the synthetic image.

The experiment in Figure 3 (b) compares the robustness of global- to structure-specific registration parameters. As expected, structure specific registration parameters are superior because they can better capture the scale differences between WHITE and GREY.

The graph in Figure 3 (c) shows the performance of an implicitly- and an explicitly-defined spatial distribution of structure BLACK. The superior implicit spatial distribution is the inverse of the spatial distribution of the aligned foreground, which is defined by WHITE and GREY. The explicit spatial distribution increases the risk of statistical inconsistency within our model. Thus, the complexity of the MAP estimation problem of Equation (11) increases, which greatly reduces the reliability of our implementation.

In summary, the most robust approach uses a hierarchical registration framework, an implicitly defined spatial background, and Powell’s method to solve the MAP estimation problem.

## 4.2 Comparative Study on 30 Test Cases

The section compares three EM implementations which differ in the mapping process of the atlas to the patient. The first approach (EM-NonRigid) maps the atlas to the patient using an intensity based non-rigid registration approach and then runs our EM implementation without registration parameters [15]. The second approach (EM-Affine) is like (EM-NonRigid) but uses the affine mapping method of Warfield et al. [19] as the

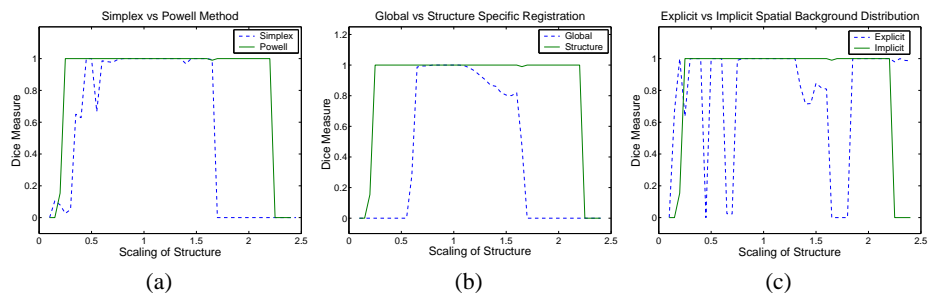


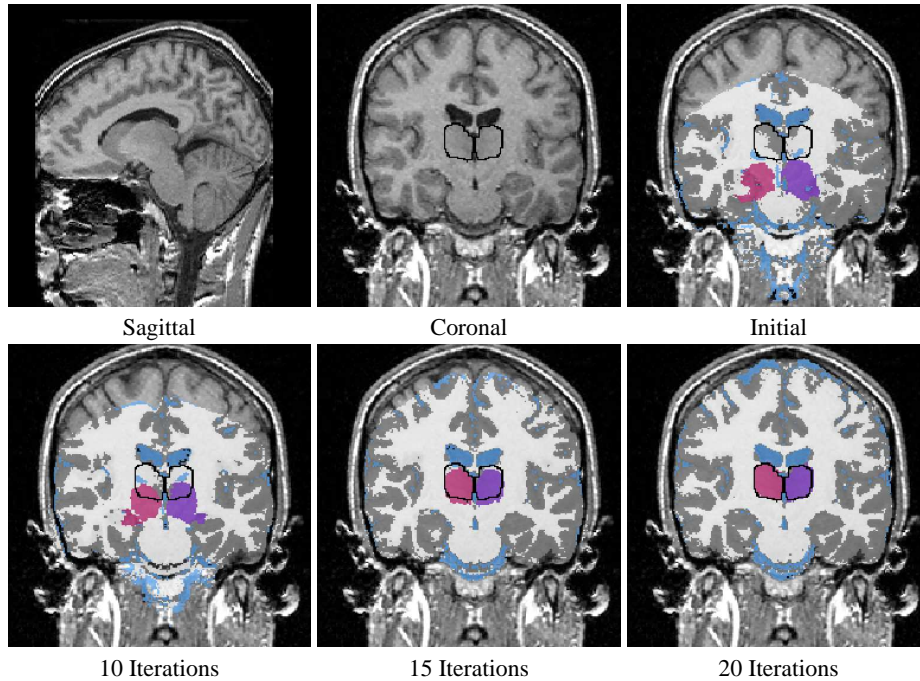
**Fig. 3.** The graphs show the robustness of implementations proposed in Section 3. The robustness of the method is determined by the quality of the automatic generated result with respect to the scaling of structure WHITE (Figure 2). The experiment suggests, that the most robust implementation uses Powell’s method to solve the MAP estimation problem (a), a hierarchical registration framework (b), and an implicitly-defined spatial distribution of the background BLACK (c).

preprocessing step. The third approach (EM-Integrated) is our novel algorithm which solves the registration and segmentation problem simultaneously.

The three methods segment 30 test cases into the three brain tissue classes and further parcellate grey matter into right and left thalamus. We compare the automatic segmentations of the thalamus to manual ones, which we view as ground-truth. We focus on the thalamus because it is a challenging structure for registration and segmentation. Many fiber tracks pass through the thalamus so that its intensity pattern in MR images is very similar to the neighboring white matter (Figure 5). Intensity based registration methods have difficulties aligning this structure because of its weakly visible boundary. In our experience EM without spatial priors will fail and EM with spatial priors heavily relies on these priors. Thus, registration errors greatly influence the segmentation quality of our three methods.

To measure the quality of the automatic generated results, we compare them to the manual segmentations using the volume overlap measure Dice. The table in Figure 5 lists the average Dice measure of the right (R Tha) and left thalamus (L Tha) for the three algorithms. In general, EM-NonRigid performed worst because the intensity based registration method is too unreliable for structures with smooth boundaries. The method often overestimates white matter and underestimated the thalamus in this region. EM-Affine performs much better than EM-NonRigid but the method is sensitive towards initial misalignments. For example, the patient shown in Figure 4 (Sagittal) has an unusually large deformation along vertical direction of the image which causes a bias along the same direction in the segmentation as shown in Figure 5 (EM-Affine).





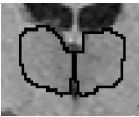


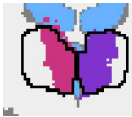
EM-Integrated was generally significantly more reliable than the other two methods (Table in Figure 5). It did not fail in any of the 30 test cases and performed equally well on the right and left thalamus. It performed much better than the other EM implementations on difficult cases, where the deformation between atlas and image space was complex. As the example of Figure 4, illustrates the accuracy of the registration and segmentation parameters greatly depend on each other. Initially, the algorithm only outlines the ventricles correctly. As the method progresses, the overall accuracy of the



**Fig. 4.** The sagittal view of the MR image shows a patient with unusually high deformation along the vertical direction. In the coronal view we outlined the right and left thalamus which was one of the structures segmented by our approach. 'Initial' is the initial segmentation of the image without atlas alignment. The results in the second row present the automatic segmentations after 10, 15, and 20 iterations. Compared to the other two methods our new approach seems to perform especially well in complicated cases like the presented one. Figure 5 shows in greater detail the segmentation of the thalamus of this patient.

registration as well as segmentation increases. In this example it took 20 iterations until the algorithm converged to the right solution and correctly segmented the thalamus whose boundary is outlined in black.

We have demonstrated that our method performs better than the methods we denoted as EM-Affine and EM-NonRigid as a consequence of the fact that our approach directly maps the spatial priors of the structures to the segmentation model. In contrast, the EM-Affine and EM-NonRigid methods align an MR image in the atlas space to the image of the patient [11], using the resulting deformation map to align the spatial priors. This inherently increases the risk of systematic biases in the model. Another explanation for the superior performance of our approach is the explicit modeling of dependency between segmentation and registration, which further constrains our implementation and thus simplifies the segmentation problem.

Avg. Dice of 30 Cases						
Method	R Tha	L Tha	Manual / SPGR	EM-Integrated	EM-Affine	EM-NonRigid
Integrated	0.870	0.869				
Affine	0.847	0.829				
NonRigid	0.754	0.783				

**Fig. 5.** The table to the left shows the mean Dice measure of the right (R Tha) and left thalamus (L Tha) over 30 test cases for the three different approaches. Our new algorithm significantly outperforms the other two, which is also visible in the pictures to the right. The images to the right zoom in on the automatic segmentations of the patient presented in Figure 4. In the MR image as well as 2D segmentations the thalamus is outlined in black.

## 5 Conclusion

We have presented a statistical framework combining inhomogeneity estimation, atlas registration, and segmentation of MR images. Unlike other voxel-based classification methods, our framework modeled these three problems as one maximization a posteriori estimation problem. We implemented the framework as an instance of an EM algorithm using a hierarchical affine mapping approach for explicit anatomical structures in combination with an implicit spatial distribution for the background. Our approach was validated by automatically segmenting 30 sets of MR images into the major brain tissue classes and the thalamus, a structure with indistinct boundaries. Using manual segmentations of the thalamus, we then compared our results to other EM implementations which sequentially register and segment. In general, our method performed significantly better than the other segmentation methods. The improvement is due primarily to the seamless integration of registration into the performance estimation problem.

*Acknowledgments:* This investigation was supported by the research grant NIH 5 P41 RR13218. We would also like to thank Corey Kemper, Sylvain Bouix and Polina Golland for their helpful comments.

## References

1. K. Pohl, S. Warfield, R. Kikinis, W. Grimson, and W. Wells, "Coupling statistical segmentation and PCA shape modeling," in *Medical Image Computing and Computer-Assisted Intervention*, vol. 3216/2004, pp. 151 – 159, 2004.
2. B. Fischl, D. Salat, E. Busa, M. Albert, M. Dieterich, C. Haselgrove, A. van der Kouwe, R. Killiany, D. Kennedy, S. Klaveness, A. Montillo, N. Makris, B. Rosen, and A. Dale, "Whole brain segmentation: Automated labeling of neuroanatomical structures in the human brain," *Neuron*, vol. 33, 2002.
3. M. Leventon, W. Grimson, and O. Faugeras, "Statistical shape influence in geodesic active contours," in *IEEE Conference on Computer Vision and Pattern Recognition*, pp. 1316 – 1323, 2000.
4. A. Tsai, A. Yezzi, W. Wells, C. Tempny, D. Tucker, A. Fan, W. Grimson, and A. Willsky, "A shape-based approach to the segmentation of medical imagery using level sets," *IEEE Transactions in Medical Imaging*, vol. 22, no. 2, pp. 137 – 154, 2003.

5. P. P. Wyatt and J. A. Noble, "MAP MRF joint segmentation and registration," in *Medical Image Computing and Computer-Assisted Intervention*, pp. 580–587, 2002.
6. C. Xiaohua, M. Brady, and D. Rueckert, "Simultaneous segmentation and registration for medical image," in *Medical Image Computing and Computer-Assisted Intervention*, pp. 663–670, 2004.
7. C. Cocosco, A. Zijdenbos, and A. Evans, "A fully automatic and robust brain MRI tissue classification method," *Medical Image Analysis*, vol. 7, pp. 513–527, 2003.
8. S. Warfield, J. Rexilius, M. Kaus, F. Jolesz, and R. Kikinis, "Adaptive, template moderated, spatial varying statistical classification," *Medical Image Analysis*, vol. 4, no. 1, pp. 43–55, 2000.
9. K. Van Leemput, F. Maes, D. Vanermeulen, and P. Suetens, "Automated model-based bias field correction of MR images of the brain," *IEEE Transactions in Medical Imaging*, vol. 18, no. 10, pp. 885–895, 1999.
10. J. Marroquin, E. Santana, and S. Botello, "Hidden markov measure field models for image segmentation," *IEEE Transactions on Pattern Analysis and Machine Intelligence*, vol. 25, pp. 1380–1387, 2003.
11. K. Pohl, W. Wells, A. Guimond, K. Kasai, M. Shenton, R. Kikinis, W. Grimson, and S. Warfield, "Incorporating non-rigid registration into expectation maximization algorithm to segment MR images," in *Medical Image Computing and Computer-Assisted Intervention*, pp. 564–572, 2002.
12. S. Srivastava, F. Maes, D. Vandermeulen, W. V. Paesschen, P. Dupont, and P. Suetens, "Effects of anatomical asymmetry in spatial priors on model-based segmentation of the brain mri: A validation study," in *Medical Image Computing and Computer-Assisted Intervention*, no. 3216 in Lecture Notes in Computer Science, pp. 327–334, Springer-Verlag, 2004.
13. W. Wells, W. Grimson, R. Kikinis, and F. Jolesz, "Adaptive segmentation of MRI data," *IEEE Transactions in Medical Imaging*, vol. 15, pp. 429–442, 1996.
14. R. Neal and G. Hinton, "A view of the EM algorithm that justifies incremental, sparse, and other variants," in *Learning in Graphical Models* (M. Jordan, ed.), pp. 355–368, Kluwer Academic Press., 1998.
15. K. Pohl, S. Bouix, R. Kikinis, and W. Grimson, "Anatomical guided segmentation with non-stationary tissue class distributions in an expectation-maximization framework," in *IEEE International Symposium on Biomedical Imaging*, pp. 81–84, 2004.
16. G. J. McLachlan and T. Krishnan, *The EM Algorithm and Extensions*. John Wiley and Sons, Inc., 1997.
17. W. Press, B. Flannery, S. Teukolsky, and W. Vetterling, *Numerical Recipes in C : The Art of Scientific Computing*. Cambridge University Press, 2 ed., 1992.
18. L.R.Dice, "Measure of the amount of ecological association between species," *Ecology*, vol. 26, pp. 297–302, 1945.
19. S. Warfield, J. Rexilius, P. Huppi, T. Inder, E. Miller, W. Wells, G. Zientara, F. Jolesz, and R. Kikinis, "A binary entropy measure to assess nonrigid registration algorithm," in *Medical Image Computing and Computer-Assisted Intervention*, pp. 266–274, Oct. 2001.